Supplementary Material for:

The potential for aqueous fluid-rock and silicate melt-rock interactions to re-equilibrate hydrogen in peridotite nominally anhydrous minerals

Kendra J. Lynn (kjlynn@udel.edu) and Jessica M. Warren

Numerical Model Setup

Our models utilize recent advances in numerical diffusion approaches that address diffusion anisotropy by allowing for high resolution investigation of diffusing species in three dimensions (c.f., Shea et al. 2015a, 2015b; Lynn et al. 2017; Krimer and Costa 2017; Jollands and Müntener 2019; Mutch et al. 2019). Previous studies have used the slowest and/or fastest crystal directions to provide maximum or minimum timescale estimates when modeling in one dimension (1D; e.g., Pan and Batiza 2002; Longpré et al. 2014; Thoraval and Demouchy 2014). However, three-dimensional modeling of compositional zoning in olivine by Shea et al. (2015b) showed that this approach results in timescales that are up to 25x longer than the true diffusion time. They advocated for a 3D volume diffusion approach that fully treats diffusion anisotropy.

The numerical models have dimensions of 221 x 221 x 221 voxels, representing olivine or pyroxene surrounded by silicate melt or aqueous fluid (Figure 3 in the main text). Different voxel sizes allowed us to test two mineral grain sizes. Voxels with a resolution of 4 x 4 x 4 μm yielded crystals that are ~1 mm along the *c*-axis and voxels of 20 x 20 x 20 μm yielded crystals that are ~3 mm along the *c*-axis.

Diffusion within the crystal volume was simulated in Matlab using finite differences and the non-concentration dependent three-dimensional form of Fick's second law (Crank 1975). This form assumes that diffusion coefficients are not sensitive to the concentration of H^+ or other elements. For isotropic calculations (e.g., as simplified for opx, for which only the [001] Arrhenius relationship is constrained), it has the form:

$$\frac{\partial C}{\partial t} = D\left[\frac{\partial^2 C}{\partial x^2} + \frac{\partial^2 C}{\partial y^2} + \frac{\partial^2 C}{\partial z^2}\right] \quad (1)$$

where C is the hydrogen concentration expressed in ppm H_2O, t (s) is time, D (m^2/s) is the diffusion coefficient for H, and x, y, and z are spatial dimensions along Cartesian coordinates.

The full numerical expressions for implementation of the models can be found in the Supplementary material of Shea et al. (2015b).

For simplicity, all numerical models are for orthorhombic crystals, where the diffusivity tensor with axes *a*, *b*, and *c* takes the form

$$D=\begin{bmatrix} D_a & 0 & 0 \\ 0 & D_b & 0 \\ 0 & 0 & D_c \end{bmatrix} \quad (2)$$

where $D_a=D_x$, $D_b=D_y$, and $D_c=D_z$ (Zhang, 2010). Modeling anisotropic diffusion (cpx and olivine) requires the following non-concentration dependent 3D form of Fick's second law:

$$\frac{\partial C}{\partial t}=\left[D_a\frac{\partial^2 C}{\partial x^2}+D_b\frac{\partial^2 C}{\partial y^2}+D_c\frac{\partial^2 C}{\partial z^2}\right] \quad (3)$$

where D_a, D_b, and D_c are the different diffusivities along the *a*-, *b*-, and *c*-axes, respectively. Comparison of cpx and opx sections in Figure S1 demonstrates the effects of anisotropic vs. isotropic diffusion.

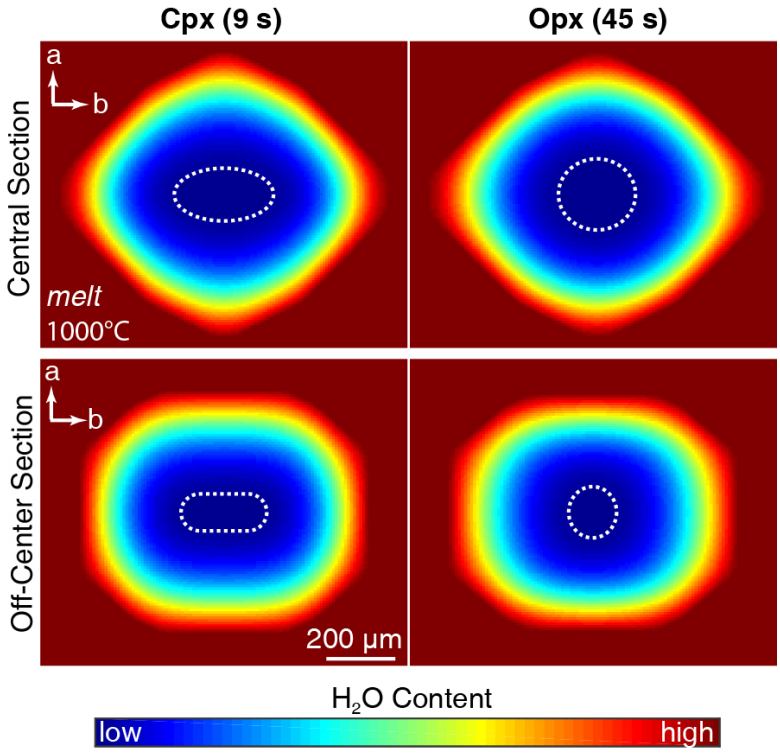

Figure S1: Examples of pyroxene models with anisotropic (Fe-bearing cpx; Woods et al. 2010; Ferriss et al. 2016) and isotropic (Fe-bearing opx with only an Arrhenius relationship for [001]; Stalder and Skogby 2003) diffusion behavior. Zonation of H_2O is scaled with color. The dashed white line represents the diffusion front, where the area inside the white line is the homogeneous core composition.

Models were initially run for two sets of boundary conditions, both of which correspond to NAM water contents in equilibrium with silicate melts outside the crystal. The "low-H" models have boundary conditions that were calculated using mineral-melt partition coefficients

from Warren and Hauri (2014) and are in equilibrium with a basaltic partial melt that has 0.75 wt% H_2O. Boundary values are 15 ppm for olivine, 135 ppm for opx, and 353 ppm for cpx (Table 1). The "high-H" models were run with the boundary condition set to the high end of the estimated water content range for each mineral in the upper mantle. Boundary values are 32 ppm for olivine, 300 ppm for opx, and 750 ppm for cpx (Hirschmann 2006; Warren and Hauri 2014). These maximum water contents correspond to a melt H_2O content of ~1.6 wt%, slightly above the range for mid-ocean ridge basalt (0.5 – 1.2 wt% H_2O; Ligi et al. 2005; Le Voyer et al. 2015; Li et al. 2017). These models allow us to evaluate the timescales over which silicate melt-rock interactions can give rise to water contents in NAMs that look similar to inferred mantle abundances.

An additional subset of cpx models was run at 800°C with higher boundary conditions to assess the sensitivity of the models to the choice of boundary condition. The experimentally determined H_2O solubility/storage capacity of NAMs varies widely with pressure, temperature, and mineral chemistry (e.g., Kohlstedt et al. 1996; Woods et al. 2000; Rauch and Keppler 2002; Stalder and Skogby 2002; Bromiley et al. 2004; Mierdel and Keppler 2004; Zhao et al. 2004; Hirschmann et al. 2005; Keppler and Bolfan-Casanova 2006; Withers and Hirschman 2008; Bali et al. 2008; Withers et al. 2011; Ferot and Bolfan-Casanova 2012; Ardia et al. 2012; Tenner et al. 2012; Demouchy and Bolfan-Casanova 2016). Most of these experiments don't include NAMs with natural mantle compositions or were conducted at pressures or temperatures too high for lithospheric conditions, thus limiting the application of solubility constraints to our determination of aqueous fluid boundary conditions here. We therefore implemented hypothetical boundary values of 10^3 and 10^4 ppm H_2O to provide an upper bound on hydrothermal fluid boundary conditions for the additional cpx models.

We track the longest possible duration that a 1-3 mm diameter grain can preserve its initial (e.g., mantle inherited) water content by sampling the central voxel of the 3D models. Most natural samples have crystal sections that are highly off-center and oblique (Figure S2), so tracking the H^+ content at the central voxel yields the most conservative estimates of re-equilibration timescales. This conservative estimate is useful for understanding the resiliency of a diffusing species to overprinting by later processes. However, non-ideal sections (i.e. off-center and oblique) of natural minerals would reflect greater degrees of re-equilibration more quickly than predicted by the core voxel (Shea et al. 2015b; Lynn et al. 2017).

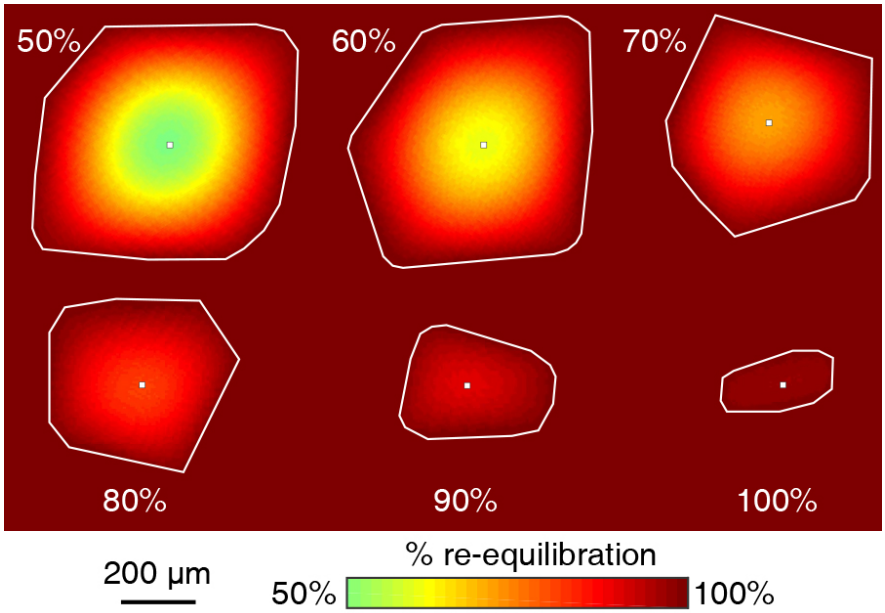

Figure S2: Numerical "thin section" of orthopyroxene slices (white outlines) taken at random orientations and distances away from the crystal core. The red background represents the boundary condition (e.g., surrounding fluid or melt). The opx crystal used for this example was taken from the high-H boundary condition model for a 1 mm diameter grain at 1000°C after 13.5 minutes of diffusive re-equilibration. The core composition was 173 ppm H_2O for the central pixel (~50% re-equilibrated). The color bar represents the compositional gradient induced by diffusion shown as % re-equilibration. The % re-equilibration sampled at the central pixel (white square) is labeled next to each slice. The 50% example is a near-ideal slice through the crystal's core, whereas the 100% example is highly off-center.

Effective %Re-equilibration

Numerical models have essentially unrestricted compositional resolution, the analytical precision of measurements in natural samples must be considered when interpreting our re-equilibration timescales as bounds on the kinetic window of hydrogen. The two main techniques for measuring H^+ in NAMs are secondary ion mass spectrometry (SIMS) and Fourier transform infrared spectroscopy (FTIR). SIMS analytical techniques and calibrations have advanced significantly in recent decades, particularly with improved methods for minimizing background water (e.g., only a few ppm) and for propagating errors (e.g., Hauri et al. 2002; Aubaud et al. 2007; Kumamoto et al. 2017). Measurements using FTIR offer the benefit of site-specific distributions of H^+ storage and diffusion pathways, but analytical resolution depends on the choice of polarized vs. unpolarized measurements, oriented vs. unoriented grains, and sample thickness (e.g., Bell et al. 2003; Aubaud et al. 2009; Stalder et al. 2012; Mosenfelder and Rossman 2013a, 2013b; Withers et al. 2012). For abyssal, opholitic, and orogenic peridotites,

NAM water contents are more commonly measured by SIMS (e.g., Gose et al. 2009; Peslier 2010; Schmädicke et al. 2011; Warren and Hauri 2014; Kumamoto et al. 2019). Thus, we utilize the analytical uncertainty from Warren and Hauri (2014) for SIMS measurements of olivine, opx, and cpx to adjust our modeled 100% re-equilibration timescales.

Individual 1D profiles of H zoning measured by SIMS may be modeled using the measured count per second ratio of $^{17}OH/^{30}Si$ or $^{1}H/^{16}O$. The additional uncertainties associated with converting count ratios to absolute concentrations can be avoided as H^+ diffusion coefficients are non-concentration dependent. The point-to-point precision of the analytical routine can be estimated from the count statistic error associated with each SIMS analysis, which is calculated from the Poisson distribution of the five-cycle count ratio average. The average count statistic error of olivine analyses in Warren and Hauri (2014) is 2 ± 1% (n=73 analyses), whereas pyroxenes are 1 ± 1% (n=250). While these count uncertainties may be small in absolute terms, they have a significant effect on our modeled timescales. Thus, we calculated an effective %re-equilibration to evaluate the resolvable re-equilibration timescales in natural samples. This parameter is calculated following Eq. 4, with the $H_{equilibrium}$ value for the boundary condition adjusted to reflect analytical uncertainties. A second effective %re-equilibration is calculated using 10% analytical error, chosen to represent reduced SIMS precision due to issues such as machine instability or variable backgrounds.

For olivine, the 2% uncertainty equates to a reduction in the resolvable boundary concentration by 0.3 and 0.6 ppm for low-H and high-H boundary conditions. This yields effective boundaries of 14.7 and 31.4 ppm, respectively, representing 96.3% and 97.6% re-equilibration (Figure S3). 10% uncertainties for the low-H and high-H boundary conditions correspond to a reduction of 1.5 and 3 ppm in resolvable boundary concentrations. This yields an effective re-equilibrated composition of 13.5 ppm H_2O or only 81% of the total % re-equilibration in our models with the low boundary condition (Figure S3). The real model diffusion time for the 1 mm olivine "total" D_H (Ferriss et al. 2018) at 1000ºC is ~6 hours, but the effective re-equilibration time at 10% uncertainty is only ~2 hours (Table S1).

For cpx, 1% SIMS uncertainty equates to a reduction in the resolvable boundary concentration by 3.5 and 7.5 ppm for the low-H and high-H boundary conditions, respectively. The effective boundary conditions become 349 and 742 ppm, corresponding to 97% and 99% re-equilibration (Table 1 in the main text). The 10% uncertainty in count statistics translates to 35 and 75 ppm for low-H and high-H boundary conditions, with the effective boundary conditions

at 315 and 675 ppm. This corresponds to 77% and 86% of the total re-equilibration determined by our low-H and high-H models, respectively (Table 1 in the main text).

For opx, an analytical error of 1% equates to a reduction in the resolvable boundary concentration by 1.4 ppm for the low-H models and 3 ppm for high-H boundary conditions. This results in effective boundaries of 133.6 and 297 ppm for low-H and high-H models, respectively, corresponding to 98.4 to 98.8% effective re-equilibration values (Table 1 in the main text, see also Table S5). At 1000 ºC for a 1 mm opx model (Figure 7 in the main text), ~98% re-equilibration corresponds to a model timescale of only 50 minutes compared to the 100% re-equilibration timescale of 72 minutes. When uncertainty in the opx water content is increased to 10%, the model uncertainty is 14 ppm for low-H and 30 ppm for high-H boundary conditions. This corresponds to 84% effective re-equilibration for the low boundary models and 88% for the high boundary models (Figure 7 in the main text). The modeled 1 mm opx timescale at 1000ºC is 72 minutes, but the effective timescales are ~25.5 minutes and ~28 minutes for the low-H and high-H silicate melt boundary conditions, respectively (see Supplementary Data File and Table S5).

Resolving diffusion profiles by SIMS or FTIR also requires good spatial resolution. In the case of SIMS, this may require that a reduced spot size is used, which will reduce the number of counts measured and thus increase analytical error. For FTIR, the spatial resolution depends both on detector setup and sample thickness (e.g., Gose et al. 2011). Hence, when spatial resolution is limited, the effective kinetic window for H re-equilibration in NAMs will similarly be reduced.

Table S5: Effective re-equilibration timescales for 1 and 3 mm minerals calculated using the low-H boundary conditions. The SIMS error timescales are calculated using 1% (cpx, opx) or 2% (ol) errors based on count statistics from measurements made by Warren and Hauri (2014). 100% re-eq timescales are the "model" columns from Table 2 in the main text for comparison. Effective timescales calculated using the high-H boundary conditions can be found in the Supplementary Data File in Table S4.

Mineral	T(°C)	100% re-eq		1% (pyx) or 2% (ol) error		10% error	
		1 mm	3 mm	1 mm	3 mm	1 mm	3 mm
Cpx PP	600	14 days	55 days	7.5 days	46 days	3.8 days	23 days
	700	1 days	8 days	17 hrs	4.4 days	8.2 hrs	2.3 days
	800	4.5 hrs	19 hrs	2.4 hrs	15 hrs	1.2 hrs	7.6 hrs
	1000	12 mins	1 hr	7.2 mins	46 mins	3.6 mins	23 mins
	1200	1.5 mins	7 mins	0.8 mins	5 mins	0.4 mins	2.5 mins
Opx PP	600	1.4 yrs	6.5 yrs	361 days	6 years	183 days	3 yrs
	700	25 days	175 days	18 days	111 days	9 days	53 days
	800	2 days	14 days	1.5 days	9.5 days	23 hrs	5 days
	1000	72 mins	7.5 hrs	52 mins	5.4 hrs	25 mins	2.8 hrs
	1200	5 mins	30 mins	3 mins	21 mins	1.7 mins	11 mins
Ol PP	600	4 days	24 days	3 days	18 days	1.4 days	8.5 days
	700	20 hrs	5 days	11 hrs	2.8 days	6.3 hrs	1.6 days
	800	4 hrs	23 hrs	2.4 hrs	15 hrs	70 mins	7.2 hrs
	1000	26 mins	2 hrs	14 mins	90 mins	7 mins	44 mins
	1200	4 mins	27 mins	2.6 mins	17 mins	1.4 mins	8.5 mins
Ol PV	600	160 yrs	1300 yrs	135 yrs	844 yrs	60 yrs	463 yrs
	700	4.9 yrs	39 yrs	9.5 yrs	37 yrs	6.2 yrs	24 yrs
	800	128 days	5 yrs	160 days	2.8 yrs	86 days	1.5 yrs
	1000	4 days	20 days	2.3 days	15 days	1.3 days	8 days
	1200	4 hrs	22 hrs	2.4 hrs	15 hrs	1.2 hrs	7.5 hrs
Ol tot	600	76 days	1 yr	44 days	274 days	22 days	134 days
	700	12 days	74 days	6.9 days	43 days	4 days	26 days
	800	2 days	14 days	1.6 days	9.8 days	19 hrs	4.8 days
	1000	6 hrs	1.5 days	3.7 hrs	23 hrs	1.9 hrs	12 hrs
	1200	1.5 hrs	7 hrs	43 mins	4.5 hrs	21 mins	2.2 hrs

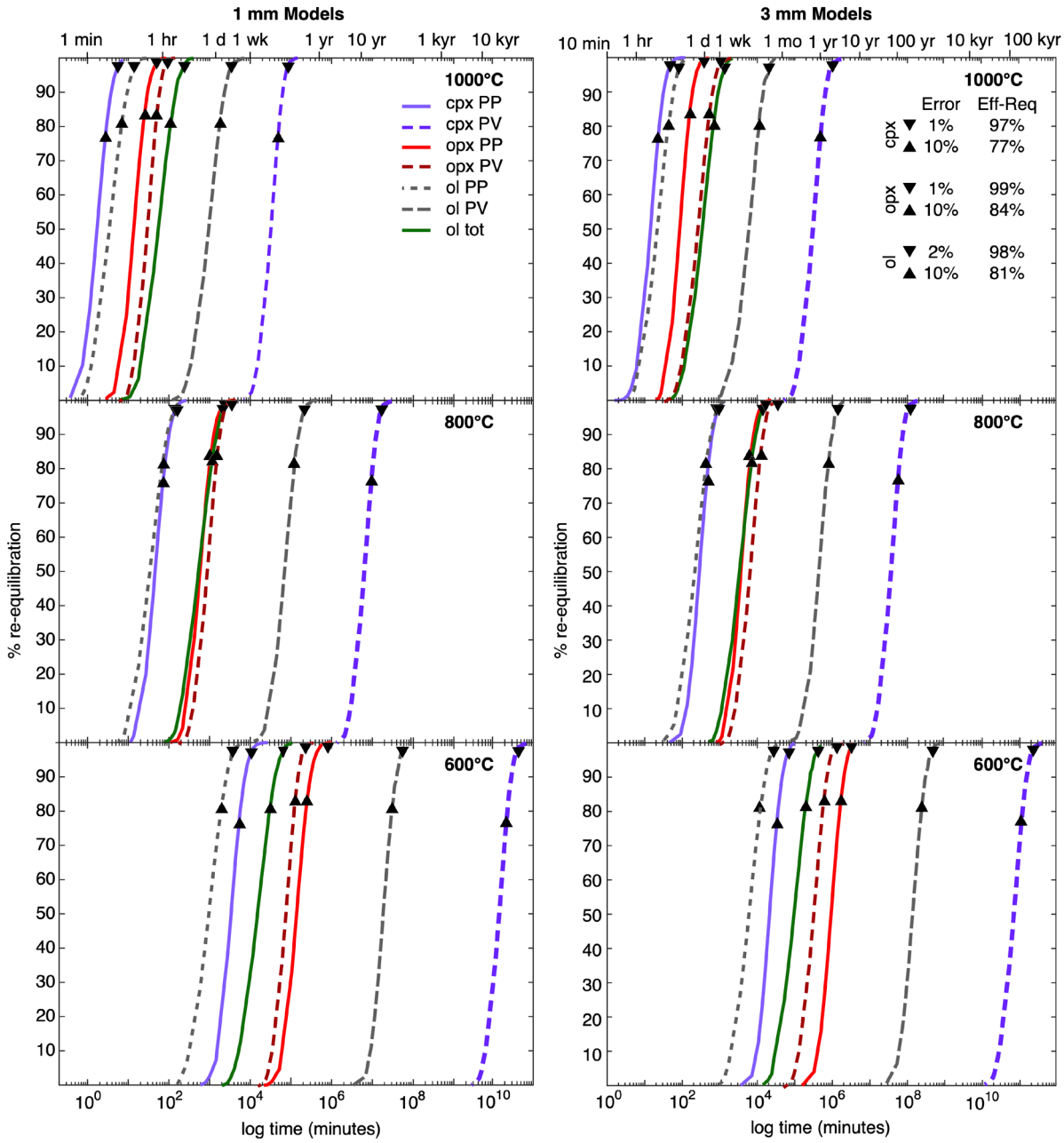

Figure S3: Detailed results of 600-1000°C models for 1-3 mm grain sizes. Each line represents the re-equilibration of the ideal core composition through time for an individual diffusion model. Clinopyroxene polaron results are shown as a solid purple line whereas vacancy results are a darker purple dashed line. Orthopyroxene polaron results are the red solid line and vacancy results are the maroon dashed line. Olivine results are as follows: total (tot) in green, olivine proton-polaron (PP) as short dashed grey lines, and olivine proton-vacancy (PV) as long dashed grey lines. Modeled timescales are plotted in log time (minutes) with conversions to common

time units at the top of the figure. Black upward pointing triangles (10% analytical error) and downward pointing triangles (1% or 2% analytical error) indicate the effective %re-equilibration point for each phase, where any zonation beyond that value would be difficult to resolve outside of analytical error.

References

Ardia, P., Hirschmann, M.M., Withers, A.C., and Tenner, T.J. (2012) H_2O storage capacity of olivine at 5-8 GPa and consequences for dehydration partial melting of the upper mantle. Earth and Planetary Science Letters, 345-348. http://dx.doi.org/10.1016/j.epsl.2012.05.038

Aubaud, C., Bureau, H., Raepsaet, C., Khodja, H., Withers, A.C., Hirschmann, M.M., and Bell, D.R. (2009) Calibration of the infrared molar absorption coefficients for H in olivine, clinopyroxene, and rhyolitic glass by elastic recoil detection analysis. Chemical Geology, 262, 78-86. https://doi.org/10.1016/j.chemgeo.2009.01.001

Aubaud, C., Withers, A.C., Hirschmann, M.H., Guan, Y., Leshin, L.A., Mackwell, S.J., and Bell, D.R. (2007) Intercalibration of FTIR and SIMS for hydrogen measurements in glasses and nominally anhydrous minerals. American Mineralogist, 92, 811-828. https://doi.org/10.2138/am.2007.2248

Bali, E., Bolfan-Casanova, N., and Koga, K.T. (2008) Pressure and temperature dependence of H solubility in forsterite: An implication to water activity in the Earth interior. Earth and Planetary Science Leters, 268, 354-363. https://doi.org/10.1016/j.epsl.2008.01.035

Bell, D.R., Rossman, G.R., Maldener, J., Endisch, D., and Rauch, F. (2003) Hydroxide in olivine: A quantitative determination of the absolute amount and calibration of the IR spectrum. Journal of Geophysical Research: Solid Earth, 108, B2. https://doi.org/10.1029/2001JB000679

Bromiley, G.D., Keppler, H., McCammon, C., Bromiley, F.A., and Jacobsen, S.D. (2004) Hydrogen solubility and speciation in natural, gem-quality chromian diopside. American Mineralogist, 89, 941-949. https://doi.org/10.2138/am-2004-0703

Crank, J. (1975) The Mathematics of Diffusion, 2nd ed.: Oxford Science Publications, Oxford, 415 p.

Demouchy, S., and Bolfan-Casanova, N. (2016) Distribution and transport of hydrogen in the lithospheric mantle: A review. Lithos, 240-243, 402-425. doi: 10.1016/j.lithos.2015.11.012

Ferot, A., and Bolfan-Casanova, N. (2012) Water storage capacity in olivine and pyroxene to 14 GPa: Implications for the water content of the Earth's upper mantle and nature of seismic discontinuities. Earth and Planetary Science Letters, 349-350, 218-230. https://doi.org/10.1016/j.epsl.2012.06.022

Ferriss, E., Plank, T., and Walker, D. (2016) Site-specific hydrogen diffusion rates during clinopyroxene dehydration. Contributions to Mineralogy and Petrology, 171, 55. https://doi.org/10.1007/s00410-016-1262-8

Gose, J., Schmädicke, E., and Stalder, R. (2011) Water in mantle orthopyroxene – no visible change in defect water during serpentinization. European Journal of Mineralogy, 23, 529-536. https://doi.org/10.1127/0935-1221/2011/0023-2122

Gose, J., Schmädicke, E., and Beran, A. (2009) Water in enstatite from Mid-Atlantic Ridge peridotite: Evidence for the water content of suboceanic mantle? Geology, 37, 543-546. https://doi.org/10.1130/G25558A.1

Hauri, E., Wang, J., Dixon, J.E., King, P.L., Mandeville, C., and Newman, S. (2002) SIMS analysis of volatiles in silicate glasses 1. Calibration, matrix effects and comparisons with FTIR. Chemical Geology, 183, 99-114. https://doi.org/10.1016/S00009-2541(01)00375-8

Hirschmann, M.M., Aubaud, C., and Withers, A.C. (2005) Storage capacity of H_2O in nominally anhydrous minerals in the upper mantle. Earth and Planetary Science Letters, 236, 167-181. https://doi.org/10.1016/j.epsl.2005.04.022

Jollands, M.C., and Müntener, O. (2019) Testing orthopyroxene diffusion chronometry on rocks from the Lanzo massif (Italian Alps). Journal of Geophysical Research: Solid Earth, 124. https://doi.org/10.1029/2018JB016963

Keppler, H., and Bolfan-Casanova, N. (2006) Thermodynamics of water solubility and partitioning. Reviews in Mineralogy and Geochemistry, 62, 193-230. https://doi.org/10.2138/rmg.2006.62.9

Kohlstedt, D.L., Keppler, H., and Rubie, D.C. (1996) Solubility of water in the alpha, beta, and gamma phases of (Mg,Fe)2SiO4. Contributions to Mineralogy and Petrology, 123, 345-357. doi: 10.1007/s004100050161

Krimer, D., and Costa, F. (2017) Evaluation of the effects of 3D diffusion, crystal geometry, and initial conditions on retrieved time-scales from Fe-Mg zoning in natural oriented orthopyroxene crystals. Geochimica et Cosmochimica Acta, 196, 271-288. https://doi.org/10.1016/j.gca.2016.09.037

Kumamoto, K.M., Warren, J.M., and Hauri, E.H. (2019) Evolution of the Josephine Peridotite shear zones: Part I: Compositional variation and shear initiation. Geochemistry Geophysics Geosystems, 20. https://doi.org/.1029/2019GC008399

Kumamoto, K.M., Warren, J.M., and Hauri, E.H. (2017) New SIMS reference materials for measuring water in upper mantle minerals. American Mineralogist, 102, 537-547. https://doi.org/10.2138/am-2017-5863CCBYNCND

Le Voyer, M., Cottrell, E., Kelley, K.A., Brounce, M., and Hauri, E.H. (2015) The effect of primary vs. secondary processes on the volatile content of MORB glasses: An example from the equatorial Mid-Atlantic Ridge (5°N-3°S). Journal of Geophysical Research: Solid Earth, 120, 125-144. https://doi.org/10.1002/2014JB011160

Li, W., Jin, Z., Li, H., and Tao, C. (2017) High water content in primitive mid-ocean ridge basalt from Southwest Indian Ridge (51.56°E): Implications for recycled hydrous component in the mantle. Journal of Earth Science, 28, 411-421. https://doi.org/10.1007/s12583-017-0731-y

Ligi, M., Bonatti, E., Cipriani, A., and Ottolini, L. (2005) Water-rich basalts at mid-ocean ridge cold spots. Nature, 434, 66-69. https://doi.org/10.1038/nature03264

Longpré, M-A., Klügel, A., Diehl, A., and Stix, J. (2014) Mixing in mantle magma reservoirs prior to and during the 2011-2012 eruption at El Hierro, Canary Islands. Geology, 42, 315-318. https://doi.org/10.1130/G35165.1

Lynn, K.J., Shea, T., and Garcia, M.O. (2017) Nickel variability in Hawaiian olivine: Evaluating the relative contributions from mantle and crustal processes. American Mineralogist, 102, 507-518. https://doi.org/10.2138/am-2017-5763.

Mierdel, K., and Keppler, H. (2004) The temperature dependence of water solubility in enstatite. Contributions to Mineralogy and Petrology, 148, 305-311. https://doi.org/10.1007/s00410-004-0605-z

Mosenfelder, J.L., and Rossman, G.R. (2013a) Analysis of hydrogen and fluorine in pyroxenes I: Orthopyroxene. American Mineralogist, 95, 1026-1041. https://doi.org/10.2138/am.2013.4291

Mosenfelder, J.L., and Rossman, G.R. (2013b) Analysis of hydrogen and fluorine in pyroxenes II: Clinpyroxene. American Mineralogist, 98, 1042-1054. https://doi.org/10.2138/am.2013.4413

Mutch, E.J.F., Maclennan, J., Holland, T.J.B., and Buisman, I. (2019) Millennial storage of near-Moho magma. Science, 356, 260-264. https://doi.org/10.1126/science.aax4092

Pan, Y., and Batiza, R. (2002) Mid-ocean ridge magma chamber processes: Constraints from olivine zonation in lavas from the East Pacific Rise at 9°30'N and 10°30'N. Journal of Geophysical Research, 107, 2022. https://doi.org/10.1029/2001JB000435.

Peslier, A.H. (2010) A review of water contents of nominally anhydrous natural minerals in the mantles of Earth, Mars, and the Moon. Journal of Volcanology and Geothermal Research, 197, 239-258. https://doi.org/10.1016/j.jvolgeores.2009.10.006

Rauch, M., and Keppler, H. (2002) Water solubility in orthopyroxene. Contributions to Mineralogy and Petrology, 143, 525-536. https://doi.org/10.1007/00410-002-0355-6

Schmädicke, E., Gose, J., and Will, T.M. (2011) Heterogeneous mantle underneath the North Atlantic: Evidence from water in orthopyroxene, mineral composition and equilibrium conditions of spinel peridotite from different locations at the Mid-Atlantic Ridge. Lithos, 125, 308-320. https://doi.org/10.1016/j.lithos.2011.02.014

Shea, T., Lynn, K.J., and Garcia, M.O. (2015a) Cracking the olivine zoning code: Distinguishing between crystal growth and diffusion. Geology, 43, 935-938. https://doi.org/10.1130/G37082.1

Shea, T., Costa, F., Krimer, D., and Hammer, J.E. (2015b) Accuracy of timescales retrieved from diffusion modeling in olivine: A 3D perspective. American Mineralogist, 100, 2026-2042. https://doi.org/10.2138/am-2015-5163

Stalder, R., and Skogby, H. (2002) Hydrogen incorporation in enstatite: European Journal of Mineralogy, 14, 1139-1144. https://doi.org/10.1127/0935-1221/2002/0014-1139

Stalder, R., and Skogby, H. (2003) Hydrogen diffusion in natural and synthetic orthopyroxene: Physics and Chemistry of Minerals, 30, 12-19. https://doi.org/10.1007/s00269-002-0285-z

Stalder, R., Prechtel, F., and Ludwig, T. (2012) No site-specific infrared absorption coefficients for OH-defects in pure enstatite. European Journal of Mineralogy, 24, 465-470.

Tenner, T.J., Hirschmann, M.M., Withers, A.C., and Ardia, P. (2012) H_2O storage capacity of olivine and low-Ca clinopyroxene from 10 to 13 GPa: consequences for dehydration melting above the transition zone. Contributions to Mineralogy and Petrology, 163, 297-316. https://doi.org/10.1007/s00410-011-0675-7

Thoraval, C., and Demouchy, S. (2014) Numerical models of ionic diffusion in one and three dimensions: applications to dehydration of mantle olivine. Physics and Chemistry of Minerals, 41, 709-723. https://doi.org/10.1007/s00269-014-0685-x

Warren, J.M., and Hauri, E.H. (2014) Pyroxenes as tracers of mantle water variations. Journal of Geophysical Research: Solid Earth, 119, 1851-1881. https://doi.org/10.1002/2013JB010328

Withers, A.C., and Hirschmann, M.M. (2008) Influence of temperature, composition, silica activity and oxygen fugacity on the H_2O storage capacity of olivine at 8 GPa. Contributions to Mineralogy and Petrology, 156, 595-605. https://doi.org/10.1007/s00410-008-0303-3

Withers, A.C., Bureau, H., Raepsaet, C., and Hirschmann, M. (2012) Calibration of infrared spectroscopy by elastic recoil detection analysis of H in synthetic olivine. Chemical Geology, 334, 92-98. https://doi.org/10.1016/j.chemgeo.2012.10.002

Withers, A.C., Hirschmann, M.M., and Tenner, T.J. (2011) The effect of Fe on olivine H_2O storage capacity: Consequences for H_2O in the martian mantle. American Mineralogist, 96, 1039-1053. https://doi.org/10.2138/am.2011.3669

Woods, S.C., Mackwell, S., and Dyar, D. (2000) Hydrogen in Diopside: Diffusion profiles. American Mineralogist, 85, 480-487. https://doi.org/10.2138/am-2000-0409

Zhang, Y. (2010) Diffusion in minerals and melts: Theoretical background. Reviews in Mineralogy and Geochemistry, 72, 5-59. https://doi.org/10.2138/rmg.2010.72.2

Zhao, Y-H., Ginsberg, S.B., and Kohlstedt, D.L. (2004) Solubility of hydrogen in olivine: dependence on temperature and iron content. Conributions to Mineralogy and Petrology, 147, 155-161.